

ARTICLE OPEN



Higher-order oscillatory planar Hall effect in topological kagome metal

Leyi Li^{1,2,4}, Enkui Yi^{1,2,4}, Bin Wang^{1,2}, Guoqiang Yu³, Bing Shen^{1,2}, Zhongbo Yan¹ and Meng Wang¹

Exploration of exotic transport behavior for quantum materials is of great interest and importance for revealing exotic orders to bring new physics. In this work, we report the observation of unconventional prominent planar Hall effect (PHE) and planar anisotropic magnetoresistivity (PAMR) in strange kagome metal KV_3Sb_5 . The PHE and PAMR, which are driven by an in-plane magnetic field and display sharp difference from other Hall effects driven by an out-of-plane magnetic field or magnetization, exhibit exotic higher-order oscillations in sharp contrast to those following empirical rule only allowing two-fold symmetrical oscillations. These higher-order oscillations exhibit strong field and temperature dependence and vanish around charge density wave (CDW) transition. The unique transport properties suggest a significant interplay of the lattice, magnetic and electronic structure in KV_3Sb_5 . This interplay can couple the hidden anisotropy and transport electrons leading to the unconventional PHE and PAMR in contrast to other materials.

npj Quantum Materials (2023)8:2; <https://doi.org/10.1038/s41535-022-00534-7>

INTRODUCTION

Planar Hall effect (PHE) is a unique transport phenomena driven by an in-plane magnetic-field-induced rotation of the principal axes of the resistivity tensor^{1,2}. Because of different origins, the PHE is in many aspects quite different from those Hall effects driven by an out-of-plane magnetic field or magnetization as shown in Fig. 1a. Obvious PHE has been observed in a few ferromagnetic metals^{1,2} and nonmagnetic semimetals with strong orbital anisotropy of electronic structure^{3,4}. It is widely used for designing and fabricating commercial magnetic sensors, especially for three-dimensional (3D) highly compacted, and ultra-sensitive 'lab-on-a-chip (LOC)' devices for the next generation chips. Another great interest for PHE lies in its angular dependence of the direction of magnetic field, which can be applied to infer the information of the underlying magnetic order or electronic structure. For example, to investigate this effect and pursue its origin in a quantum system may reveal nontrivial topological physics or reveal the exotic states and orders to advance the understanding of fundamental physics^{5–10}.

Recently, superconductivity was observed in a new family of layered kagome metals AV_3Sb_5 ($A = K, Rb, Cs$)^{11–16}. Their normal states are identified as Z_2 topological metals with multiple topologically nontrivial band structures such as flat band, van Hove singularity, and Dirac-fermion dispersion in close proximity to the Fermi level^{17–22}. In the absence of magnetism, it is surprising to observe a giant anomalous Hall effect (AHE) in these materials. To reconcile the observations, the AHE is considered to strongly correlate to novel orders such as chiral charge-density-wave (CDW) or nematic order accompanying with symmetry breaking^{23–31}. However, because the correlations among spin, charge, lattice, and other orders are expected to be important, it remains a great challenge to get a full understanding of the origin of the various novel transport properties observed in this family of materials. In this work, we observe

prominent PHE and planar anisotropic magnetoresistivity (PAMR) in KV_3Sb_5 . More interestingly, below the CDW transition the in-plane applied magnetic field drives exotic higher-order oscillations for PHE and PAMR violating the empirical law in former materials (even in recent topological materials). The unique behaviors exhibit strong field response accompanying with non-monotonous anisotropic field dependent in-plane resistivity. These abnormal planar transport properties suggest a strong coupling between transport electrons and anionotropies from the system with various orders in contrast to other materials. By scrutinizing various possible mechanisms, we suggest a significant interplay of the lattice, magnetism, and electron associated with the fluctuations as the media leading to those unconventional transport behavior.

RESULTS

Conventional planar Hall effect PHE and PAMR

As shown in Fig. 1a, the PHE and PAMR can be characterized by measuring the transverse resistivity (ρ_{xy}) and longitudinal resistivity (ρ_{xx}) with applying an in-plane magnetic field (rotating within the ab plane of KV_3Sb_5 shown in Fig. 1b) which fails to drive the ordinary Hall effect (OHE) measured with an out-of-plane magnetic field. Usually, obvious PHE and PAMR are only observed in a few kinds of materials and follow the angular dependence as:

$$\rho_{xy} = -\Delta\rho \sin\theta \cos\theta, \quad (1)$$

$$\rho_{xx} = \rho_{\perp} - \Delta\rho \cos^2\theta, \quad (2)$$

where ρ_{xy} represents the in-plane Hall resistivity that directly shows the PHE, ρ_{xx} is the PAMR, and $\Delta\rho = \rho_{\perp} - \rho_{\parallel}$ is the resistivity anisotropy (called chiral resistivity in topological materials) with ρ_{\perp} and ρ_{\parallel} representing the resistivity with the applied field $\mu_0 H$ perpendicular (90°) and parallel (0°) to the electric current respectively¹. According to these formulas, angular dependent

¹Center for Neutron Science and Technology, Guangdong Provincial Key Laboratory of Magnetoelectric Physics and Devices, School of Physics, Sun Yat-Sen University, Guangzhou, Guangdong 510275, China. ²State Key Laboratory of Optoelectronic Materials and Technologies, Sun Yat-Sen University, Guangzhou, Guangdong 510275, China. ³Beijing National Laboratory for Condensed Matter Physics, Institute of Physics, University of Chinese Academy of Sciences, Chinese Academy of Sciences, Beijing 100190, China. ⁴These authors contributed equally: Leyi Li, Enkui Yi. ✉email: shenbing@mail.sysu.edu.cn; yanzhb5@mail.sysu.edu.cn; wangmeng5@mail.sysu.edu.cn

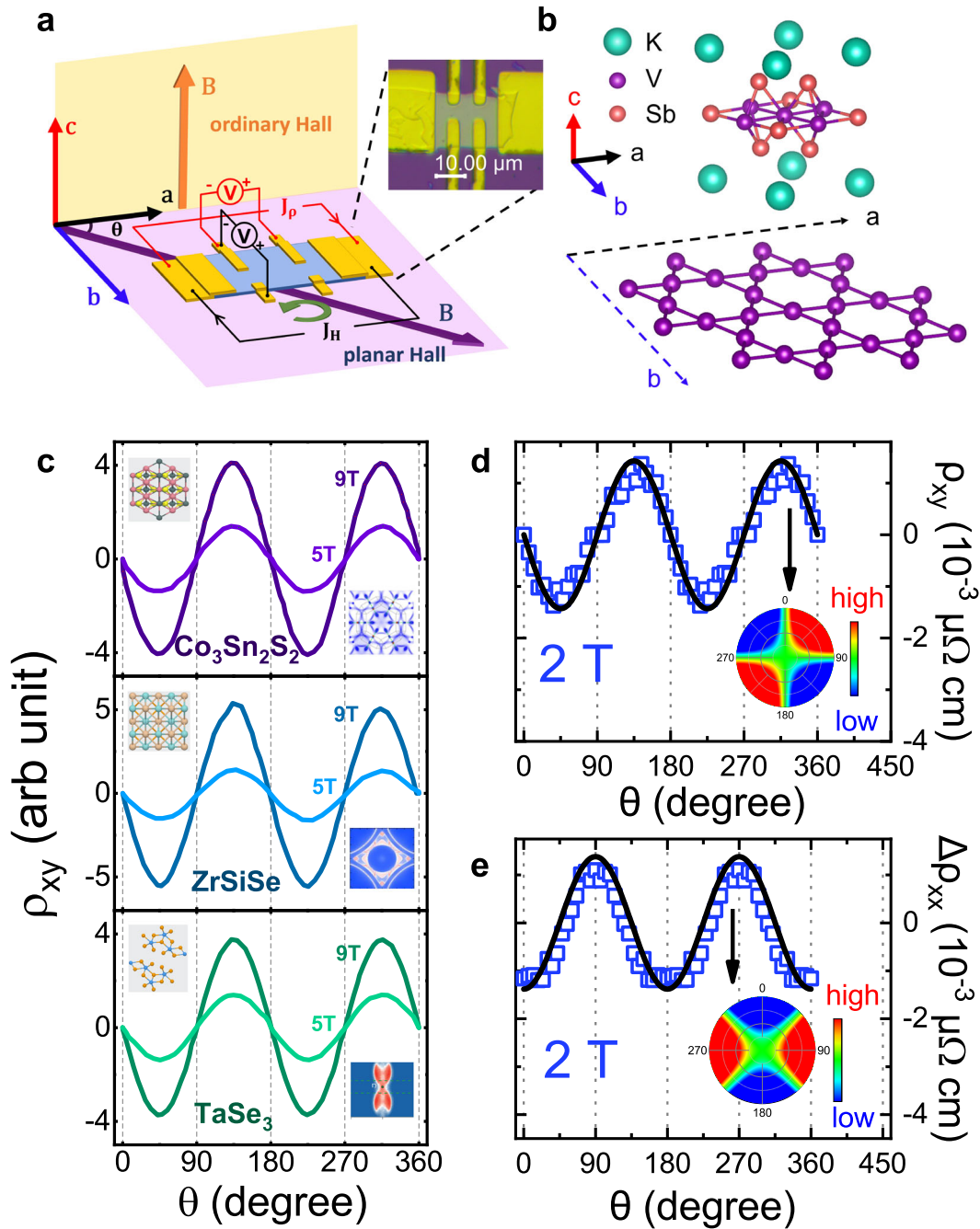


Fig. 1 Schematics and typical results of the measurements for PHE and PAMR. **a** Schematic of the geometry of the device in our measurements for the ordinary Hall, planar Hall, and longitudinal resistivity. Inset: the picture of our device. **b** Crystal structure of KV_3Sb_5 . θ is defined as the angle between the directions of current and in-plane applied field. For our device, the current is along a axis. **c** The PHE in $\text{Co}_3\text{Sn}_2\text{S}_2$, ZrSiSe , and TaSe_3 ^{32–37}. The insets: the crystal structure and Fermi surface in these three materials. **d, e** $\rho_{xy}(\theta)$ and $\rho_{xx}(\theta)$ with $\mu_0H = 2$ T at 10 K marked by blue open squares. The black solid lines indicate the $\rho_{xy}(\theta)$ and $\rho_{xx}(\theta)$ for conventional PHE and PAMR described by formula 1 and 2 respectively, which are also plotted in the insets exhibiting two-fold symmetry by the color contours in polar coordinates where the r axes are $\rho_{xy}(\theta)$ and $\rho_{xx}(\theta)$ respectively, and θ is the rotating angle defined in (a).

ρ_{xy} ($\rho_{xy}(\theta)$) and ρ_{xx} ($\rho_{xx}(\theta)$) exhibit twofold oscillations and a relative 45°-angle shift for $\rho_{xy}(\theta)$ and $\rho_{xx}(\theta)$ as shown in Fig. 1d, e^{32–37}. It is observed that the anisotropy from lattice, magnetism, or Fermi surface, etc usually hardly affect the in-plane transport behavior such as PHE and PAMR. For KV_3Sb_5 , obvious PHE and PAMR are observed at 2 K even with a small applied field of $\mu_0H = 2$ T after subtracting the OHE and out-of-plane magneto resistivity^{9,13}. ρ_{xy} and ρ_{xx} (shown in Fig. 1d, e) exhibit two-fold symmetrical oscillations and roughly follow the

conventional angular dependence. The little discrepancy between our results and empirical formulas can be attributed to the existence of additional higher-order oscillations (discussed below).

Higher-order oscillatory planar Hall effect

With increasing the applied field (μ_0H), as shown in Fig. 2, at 2 K additional features are observed in ρ_{xy} at 90° and 270° with $\mu_0H = 7$ T accompanying with the emergence of additional small

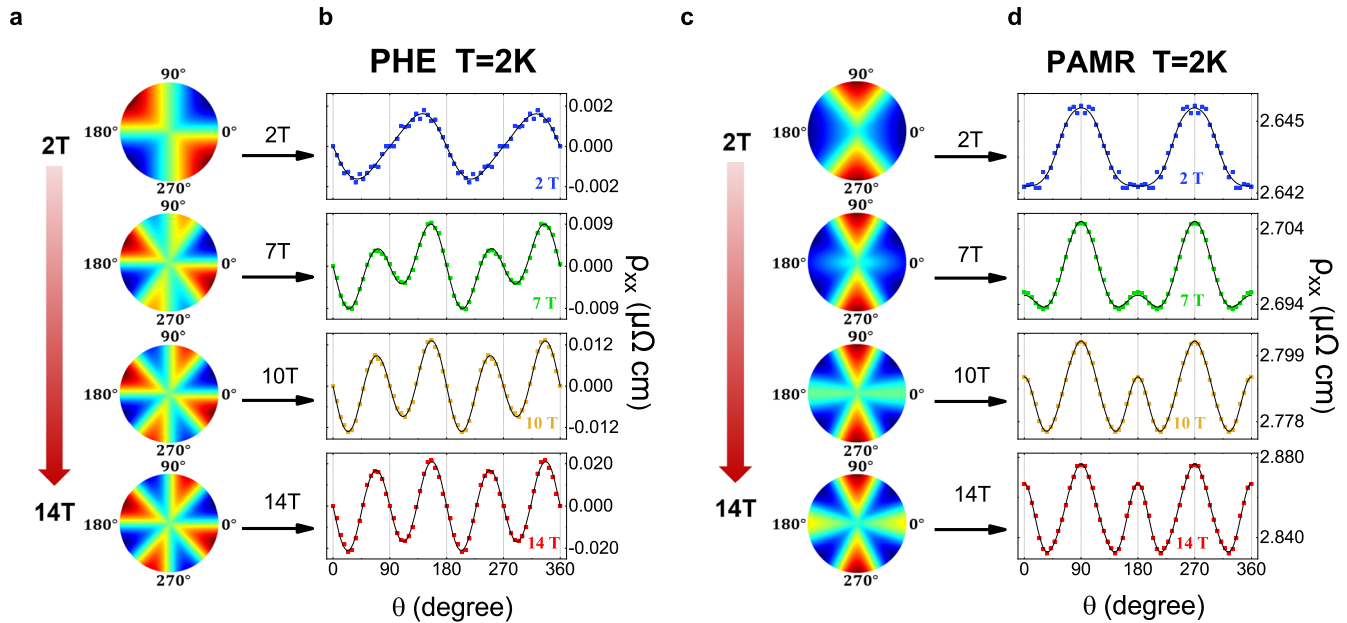


Fig. 2 PHE and PAMR for KV_3Sb_5 at 2 K. **a, c** The 2D color plots for PHE and PAMR at 2 K with $\mu_0H = 2, 7, 10,$ and 14 T respectively in the polar coordinates where r represents the applied field, θ is the rotating angle, the red region represents higher resistivity, and the blue region represents lower resistivity. **b, d** The related data of $\rho_{xy}(\theta)$ and $\rho_{xx}(\theta)$ from (a, c). The experimental data are marked by open symbols and the fitting curves by formulas 3 and 4 marked by solid lines.

peaks in $\rho_{xx}(\theta)$ at 0° and 180° . With further increasing μ_0H to 14 T, the oscillations of both $\rho_{xy}(\theta)$ and $\rho_{xx}(\theta)$ exhibit prominent higher-order oscillatory components in sharp contrast to those for conventional PHE and PAMR with only two-fold symmetrical oscillations. To investigate these phenomena, Fast Fourier transform (FFT) is applied for $\rho_{xy}(\theta)$ and $\rho_{xx}(\theta)$ at 2 K with various applied fields as shown in Fig. 3a, b. Besides the peaks at 180° in FFT spectrum relating to two-fold symmetrical oscillations, another obvious peaks at 90° are observed at high fields whose amplitude is larger than those at 180° , indicating the appearance of four-fold symmetrical oscillations. With decreasing μ_0H , these four-fold symmetrical oscillations become weaker and their amplitudes shrink to the value smaller than those with two-fold symmetry at $\mu_0H = 5$ T shown in Fig. 3c, d. With decreasing μ_0H to 2 T, the FFT peaks at 90° are much weaker than those at 180° , indicating the oscillations mainly containing two-fold symmetry component. In addition, small peaks are observed at 60° in the FFT spectrum for $\rho_{xx}(\theta)$, suggesting the appearance of six-fold symmetrical oscillation which are much weaker than the two-fold and four-fold symmetrical oscillations. To gain more clues on the emergence of higher-order oscillatory components, the field dependent Hall and longitudinal resistivity $\rho_{xy}(H)$ and $\rho_{xx}(H)$ are measured with rotating an in-plane applied field at angles from 0° to 90° shown in Fig. 3e, f. In these color contour plots, it is clearly observed that minimums appear around 45° and 20° for $\rho_{xy}(H)$ and $\rho_{xx}(H)$ at high fields, respectively, which is consistent with the emergence of additional higher-order oscillatory components (especially the four-fold symmetrical oscillatory components) in our former results and analysis for $\rho_{xy}(\theta)$ and $\rho_{xx}(\theta)$.

Figure 4a, b present the temperature dependence of $\rho_{xy}(\theta)$ and $\rho_{xx}(\theta)$ with $\mu_0H = 14$ T, respectively. By the similar FFT analysis shown in Fig. 4c, d, it is observed that the high-order oscillatory components relating to the four-fold symmetrical oscillation appear below the CDW transition (identified by an anomaly in temperature-dependent resistivity along c axis around 80 K here), and increase obviously with decreasing the temperature, as shown in Fig. 4e. Above 80 K, the oscillations of $\rho_{xy}(\theta)$ and $\rho_{xx}(\theta)$ only contain two-fold symmetrical oscillatory component and can

be well described by empirical formulas 1 and 2. To pursue the origin of the observed unconventional PHE and PAMR, we first carefully check the extrinsic contributions, such as current jetting effect due to the inhomogeneous current distribution³⁸. The possible tiny current distortion in our devices is difficult to drive additional prominent oscillations here (see Supplemental Fig. 2). The intrinsic origins usually can be (1) the spin-dependent scattering due to the classical orbital magnetism or the interactions of the magnetic order and the spin-orbit coupling³⁸, (2) chiral anomaly in a nonmagnetic topological system⁵, and (3) anisotropically lifting the protection of surface Dirac fermions from backscattering in a topological insulator¹⁰. However, these mechanisms can only host to the two-fold symmetrical oscillations for PHE and PAMR obeying the conventional formulas (1) and (2) and fail to result in high-order oscillatory components.

DISCUSSION

Usually the additional anisotropy from a system is difficult to behave in conventional PHE and PAMR even the system hosts high anisotropic Fermi surface, magnetism, or lattice such as in kagome magnet $Co_3Sn_2S_2$, tetragonal $ZrSiSe$, and quasi-one dimensional $TaSe_3$ ^{32–37}. However, these additional anisotropies should be considered in KV_3Sb_5 . The anisotropic Fermi surfaces (triangular-shaped pockets) are observed around M point²⁷, but the shape of the Fermi surface changes little in the presence of CDW order and higher-order oscillatory PHE and PAMR, which is unlikely to bring the appearance of large anisotropy in carrier density and scattering rate directly. Thus the mechanism applied to explain the higher-order oscillations in materials such as bismuth or (111) $LaAlO_3/SrTiO_3$ oxide interface^{4,39,40} is not applicable. In KV_3Sb_5 no long-range or short-range magnetic orders were observed, thus the anisotropy from conventional static magnetic order also seems not applicable. In semi-class model, the resistivity comes from the electron scattering with the lattice. Thus the anisotropy of the lattice can naturally host anisotropic carrier scattering with constrictions of the lattice's symmetry. It is noticed that even in presence of some distortion

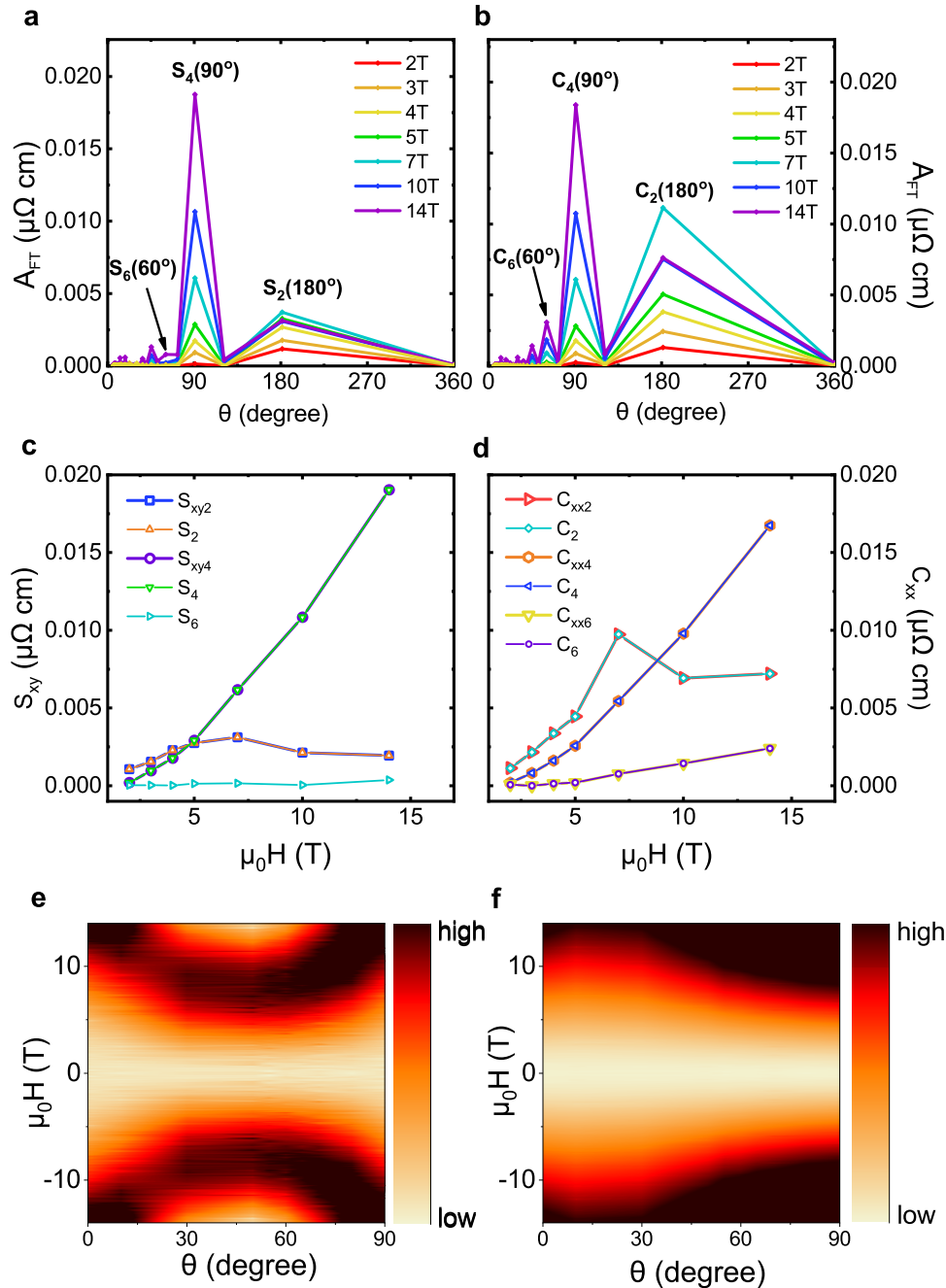


Fig. 3 The analysis of symmetry for oscillatory PHE and PAMR. **a, b** The Fast Fourier Transform (FFT) spectrum of $\rho_{xy}(\theta)$ and $\rho_{xx}(\theta)$ at 2 K with $\mu_0H = 2, 3, 4, 5, 7, 10,$ and 14 T. **c, d** The field dependence of high-order oscillatory coefficients for PHE and PAMR. $S_2, S_4, S_6, C_2, C_4,$ and C_6 are acquired from the amplitude of peaks of FFT spectrum of **(a, b)**. $S_{xy2}, S_{xy4}, C_{xx2}, C_{xx4},$ and C_{xx6} are acquired from the data fitting for the formulas (3) and (4). **e, f** The color plots for field dependent planar Hall and longitudinal resistivity $\rho_{xy}(\mu_0H)$ and $\rho_{xx}(\mu_0H)$ at the angles from 0° to 90° with the step of 10° .

due to the CDW the lattice for KV_3Sb_5 still keeps hexagonal structure. In the two dimensional case with C_6 rotation invariance³⁹, $\rho_{xy}(\theta)$ and $\rho_{xx}(\theta)$ can be expressed as:

$$\rho_{xy} = S_{xy2} \sin(2\theta - 2\phi) + S_{xy4} \sin(4\theta + 2\phi), \quad (3)$$

$$\rho_{xx} = C_{xx0} + C_{xx2} \cos(2\theta - 2\phi) + C_{xx4} \cos(4\theta + 2\phi) + C_{xx6} \cos 6\theta, \quad (4)$$

where $S_{xy2}, C_{xx2}, S_{xy4}, C_{xx4},$ and C_{xx6} are the coefficients for two, four, and six -fold symmetrical oscillations for PHE and PAMR

related to lattice symmetry³⁹ (see Supplementary Note 4). ϕ is the angle between the current I and a axis and here $\phi = 0$ with $I // a$. By using these formulas, the our data can be well fitted in consisted with former FFT analysis. Above CDW transition $S_{xy4}, C_{xx4},$ and C_{xx6} become to zero, the formula 3 and 4 become to formula 1 and 2 respectively indicating the PHE and PAMR obeying the conventional empirical law. Below the CDW transition, $S_{xy4}, C_{xx4},$ and C_{xx6} increase with the decreasing temperature and exhibit a strong field response with more contributions for oscillatory ρ_{xy} and ρ_{xx} at high fields. The temperature and field

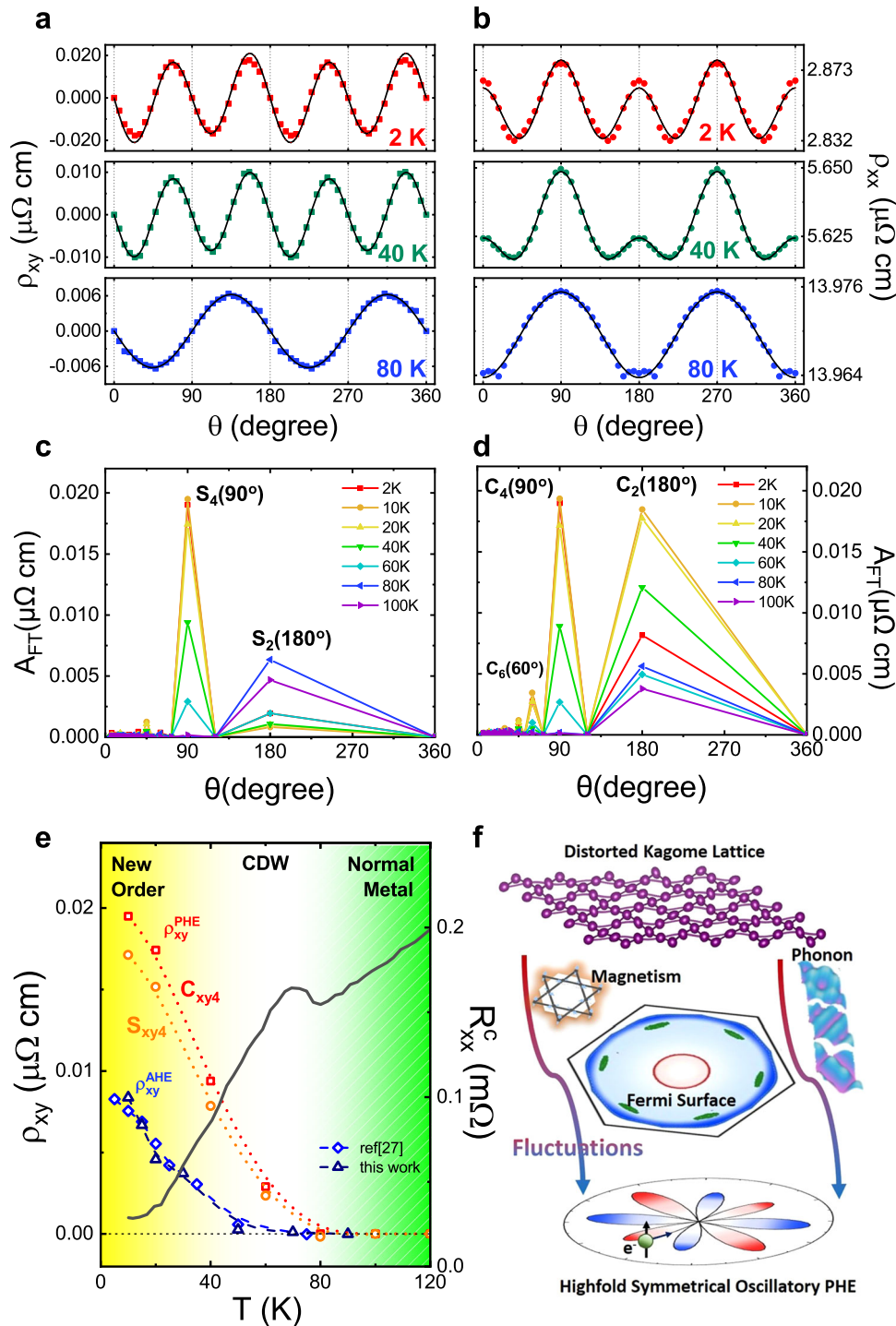


Fig. 4 The phase diagram for evolved high-order components of PHE and PAMR. **a, b** The typical $\rho_{xy}(\theta)$ and $\rho_{xx}(\theta)$ with $\mu_0H = 14$ T at 2, 40, and 80 K. The fitting curves are marked by black solid lines. **c, d** The FFT spectrum of $\rho_{xy}(\theta)$ and $\rho_{xx}(\theta)$ with $\mu_0H = 14$ T at 2, 10, 20, 40, 60, 80, and 100 K, respectively. **e** The temperature dependent anomalous Hall resistivity ρ_{xy}^{AHE} for two samples are shown with the left axis. The data of black line are acquired from our measurements and the data of blue line are acquired from ref. ²⁷. The temperature dependent S_{xy4} and C_{xx4} for ρ_{xy} are also shown with the left axis. The temperature dependent resistance along c axis R_{xx}^c is shown with the right axis with a prominent CDW anomaly around 78 K. **f** The schematic for the coupling between distorted lattice and Fermi surface leading to high symmetrical oscillatory PHE driven by an in-plane field.

dependence of high-order oscillatory components (S_{xy4} , C_{xx4} , and C_{xx6}) suggests the strong enhancement of a unique coupling between anisotropy from lattice and electrons scattering for planar transport behavior. Besides, recently, we also noticed the observation for possible domains for three nematic orders, which

may also bring the additional anisotropies for the abnormal PHE and PAMR⁴¹.

Accompanying with CDW transition, it is observed that obvious multiple fluctuations emerge simultaneously. From lattice side, strong phononic fluctuations were revealed accompanying with

lattice distortions⁴². From the electronic side, the electronic instability can host electronic fluctuations (including the nematic fluctuations) and result in electronic nematicity at lower temperatures with symmetry reduction⁴³. Moreover, from magnetism side, for KV₃Sb₅ though in absence of long-range or short range magnetic order, the magnetic fluctuations due to observed orbital ordering would inherit the crystalline anisotropy of the kagome lattice which plays a crucial role in the magnetic properties, especially for the appearance of time-reversal symmetry breaking. We find that the observed $\rho_{\parallel} < \rho_{\perp}$ (see Fig. 2) is consistent with this picture since a magnetic field will suppress magnetic fluctuations in the field direction. In fact, these fluctuations are correlated and can origin from same instability due to CDW transition indicating presence of multiple orders in the system. These correlated fluctuations can be attributed to mediate the crystalline anisotropy and electron scatterings for planar resistivity tensors to behave higher-order oscillatory components (as shown in Fig. 4f) revealing a unique interplay of lattice, electron and magnetism in KV₃Sb₅.

In summary, prominent PHE and PAMR are observed in KV₃Sb₅. The applied field would drive higher-order oscillations for both ρ_{xy} and ρ_{xx} below the CDW transition, resulting in the violation of the empirical law. This exotic phenomena suggests a strong and complicated coupling between lattice symmetry and electron scatterings for planar transport properties. We expect that such unconventional PHE and PAMR are not only potential for next generation 3D chips, but also reveal a unique interplay between various degrees of freedom for materials with frustrated crystal structures, lattice distortions and anisotropic magnetic fluctuations.

METHODS

Single crystals preparation

Single crystals of KV₃Sb₅ were grown via the self-flux method. K, V and Sb were mixed by the ratio of 1:1:4.5 and sealed inside a Ta crucible. This Ta crucible was subsequently inside in evacuated quartz tube. The mixture was heated to 1000 °C, slowly cooled to 700 °C, and finally decanted by a centrifuge. Planar single crystals with typical dimensions of 2 × 3 × 0.3 mm³ were harvested at the bottom of the crucible.

Crystal structure characterization

Crystal structure and elemental composition were confirmed by X-ray diffraction (XRD) and energy dispersive spectrometer (EDS). Sharp peaks in the XRD confirm high crystalline quality of the samples.

Device fabrication

The Hall-bar devices were fabricated by exfoliating the single crystal of KV₃Sb₅ on to a SiO₂/Si substrate. Electronic contacts were added via patterned mask with photolithography subsequent growth of Ti/Au(10 nm/100 nm) layers. Electrical transport measurements were performed in a Physical Properties Measurement System (PPMS Dynacool, Quantum design). Direct current (DC) magnetization and alternating current (AC) susceptibility measurements were performed in a Magnetic Property Measuring System (MPMS Quantum design).

DATA AVAILABILITY

The data supporting the findings of this study are available within the paper and in the Supplementary Information, and also are available from the corresponding authors upon reasonable request.

Received: 21 July 2022; Accepted: 15 December 2022;

Published online: 07 January 2023

REFERENCES

- Koch, K. M. Notizen: Zum Problem der galvanomagnetischen Effekte in ferromagnetischen. *Z. Naturforsch. A* **10**, 496 (1955).
- Goldberg, C. & Davis, R. E. New galvanomagnetic effect. *Phys. Rev.* **94**, 1121 (1954).
- Liu, Q. Nontopological origin of the planar Hall effect in the type-II Dirac semimetal NiTe₂. *Phys. Rev. B* **99**, 155119 (2019).
- Yang, S.-Y., Chang, K. & Parkin, S. S. P. Large planar Hall effect in bismuth thin films. *Phys. Rev. Res.* **2**, 022029 (2020).
- Burkov, A. A. Giant planar Hall effect in topological metals. *Phys. Rev. B* **96**, 041110 (2017).
- Nandy, S., Sharma, G., Taraphder, A. & Tewari, S. Chiral anomaly as the origin of the planar Hall effect in Weyl semimetals. *Phys. Rev. Lett.* **119**, 176804 (2017).
- Li, H., Wang, H.-W., He, H., Wang, J. & Shen, S.-Q. Giant anisotropic magnetoresistance and planar Hall effect in the Dirac semimetal Cd₃As₂. *Phys. Rev. B* **97**, 201110 (2018).
- Chen, F. C. et al. Planar Hall effect in the type-II Weyl semimetal T_r-MoTe₂. *Phys. Rev. B* **98**, 041114 (2018).
- Kumar, N., Guin, S. N., Felser, C. & Shekhar, C. Planar Hall effect in the Weyl semimetal GdPtBi. *Phys. Rev. B* **98**, 041103 (2018).
- Taskin, A. A. et al. Planar Hall effect from the surface of topological insulators. *Nat. Commun.* **8**, 1340 (2017).
- Ortiz, B. R. et al. New kagome prototype materials: discovery of KV₃Sb₅, RbV₃Sb₅, and CsV₃Sb₅. *Phys. Rev. Mater.* **3**, 094407 (2019).
- Ortiz, B. R. et al. Superconductivity in the \mathbb{Z}_2 kagome metal KV₃Sb₅. *Phys. Rev. Mater.* **5**, 034801 (2021).
- Yin, Q. et al. Superconductivity and normal-state properties of Kagome metal RbV₃Sb₅ single crystals. *Chin. Phys. Lett.* **38**, 037403 (2021).
- Chen, K. Y. et al. Double superconducting dome and triple enhancement of T_c in the kagome superconductor CsV₃Sb₅ under high pressure. *Phys. Rev. Lett.* **126**, 247001 (2021).
- Du, F. et al. Pressure-induced double superconducting domes and charge instability in the kagome metal KV₃Sb₅. *Phys. Rev. B* **103**, L220504 (2021).
- Zhang, Z. et al. Pressure-induced reemergence of superconductivity in the topological kagome metal CsV₃Sb₅. *Phys. Rev. B* **103**, 224513 (2021).
- Ortiz, B. R. et al. CsV₃Sb₅: a \mathbb{Z}_2 topological kagome metal with a superconducting ground state. *Phys. Rev. Lett.* **125**, 247002 (2020).
- Kiesel, M. L., Platt, C. & Thomale, R. Unconventional Fermi surface instabilities in the kagome Hubbard model. *Phys. Rev. Lett.* **110**, 126405 (2013).
- Wang, W.-S., Li, Z.-Z., Xiang, Y.-Y. & Wang, Q.-H. Competing electronic orders on kagome lattices at van Hove filling. *Phys. Rev. B* **87**, 115135 (2013).
- Feng, X., Jiang, K., Wang, Z. & Hu, J. Chiral flux phase in the kagome superconductor AV₃Sb₅. *Sci. Bull.* **66**, 1384 (2021).
- Denner, M. M., Thomale, R. & Neupert, T. Analysis of charge order in the kagome metal AV₃Sb₅ (A = K, Rb, Cs). *Phys. Rev. Lett.* **127**, 217601 (2021).
- Li, H. et al. Observation of unconventional charge density wave without acoustic phonon anomaly in kagome superconductors AV₃Sb₅ (A = Rb, Cs). *Phys. Rev. X* **11**, 031050 (2021).
- Jiang, Y.-X. et al. Unconventional chiral charge order in kagome superconductor KV₃Sb₅. *Nat. Mater.* **20**, 1353 (2021).
- Wang, Z. et al. Electronic nature of chiral charge order in the kagome superconductor CsV₃Sb₅. *Phys. Rev. B* **104**, 075148 (2021).
- Zhao, H. et al. Cascade of correlated electron states in the kagome superconductor CsV₃Sb₅. *Nature* **599**, 216 (2021).
- Chen, H. et al. Roton pair density wave in a strong-coupling kagome superconductor. *Nature* **599**, 222 (2021).
- Yang, S.-Y. et al. Giant, unconventional anomalous Hall effect in the metallic frustrated magnet candidate, KV₃Sb₅. *Sci. Adv.* **6**, eabb6003 (2020).
- Li, H. et al. Rotation symmetry breaking in the normal state of a kagome superconductor KV₃Sb₅. *Nat. Phys.* **18**, 265–2703 (2022).
- Yu, F. H. et al. Concurrence of anomalous Hall effect and charge density wave in a superconducting topological kagome metal. *Phys. Rev. B* **104**, L041103 (2021).
- EM, K., BR, O., C, W., SD, W. & MJ, G. Absence of local moments in the kagome metal KV₃Sb₅ as determined by muon spin spectroscopy. *J. Phys. Condens. Matter* **33**, 235801 (2021).
- Yu, L. et al. Evidence of a hidden flux phase in the topological kagome metal CsV₃Sb₅. Preprint at <https://arxiv.org/abs/2107.10714> (2021).
- Yang, S. Y. et al. Field-modulated anomalous Hall conductivity and planar Hall effect in Co₃Sn₂S₂ nanoflakes. *Nano Lett.* **20**, 7860 (2020).

33. Xu, Q. et al. Topological surface Fermi arcs in the magnetic Weyl semimetal $\text{Co}_3\text{Sn}_2\text{S}_2$. *Phys. Rev. B* **97**, 235416 (2018).
34. Chen, F. C. et al. Temperature-induced Lifshitz transition and possible excitonic instability in ZrSiSe . *Phys. Rev. Lett.* **124**, 236601 (2020).
35. Wei, B., Bu, H., Zhang, S. & Song, F. Observation of planar Hall effect in topological semimetal ZrSiSe device. *Acta Phys. Sin.* **68**, 227203 (2019).
36. Yang, X. C. et al. Planar Hall effect in the quasi-one-dimensional topological superconductor TaSe_3 . *Phys. Rev. B* **104**, 155106 (2021).
37. Gatti, G. et al. Origin of large magnetoresistance in the topological non-symmorphic semimetal TaSe_3 . *Phys. Rev. B* **104**, 155122 (2021).
38. Liang, S. et al. Experimental tests of the chiral anomaly magnetoresistance in the Dirac–Weyl semimetals Na_3Bi and GdPtBi . *Phys. Rev. X* **8**, 031002 (2018).
39. Rout, P. K., Agireen, I., Maniv, E., Goldstein, M. & Dagan, Y. Six-fold crystalline anisotropic magnetoresistance in the (111) $\text{LaAlO}_3/\text{SrTiO}_3$ oxide interface. *Phys. Rev. B* **95**, 241107 (2017).
40. Yamada, A. & Fuseya, Y. Angular dependence of magnetoresistance and planar Hall effect in semimetals in strong magnetic fields. *Phys. Rev. B* **103**, 125148 (2021).
41. Xu, Y. et al. Three-state nematicity and magneto-optical Kerr effect in the charge density waves in kagome superconductors. *Nat. Commun.* **18**, 1470–1475 (2022).
42. Alaska, S. Hexagonal-to-base-centered-orthorhombic 4Q charge density wave order in kagome metals KV_3Sb_5 , RbV_3Sb_5 , and CsV_3Sb_5 . *Phys. Rev. Mater.* **6**, 015001 (2022).
43. Li, H. et al. Conjoined charge density waves in the kagome superconductor CsV_3Sb_5 . *Nat. Commun.* **13**, 6348 (2022).

ACKNOWLEDGEMENTS

Works are supported by National Natural Science Foundation of China (NSFC) (Grants Nos. U2130101, 92165204, 12174454, 12174455, and 11904417), Guangzhou Basic and Applied Basic Research Foundation (Grant Nos. 2022A1515010035, 2021B1515020026, 2021B1515120015), Guangzhou Basic and Applied Basic Research Foundation (Grant No. 202201011798), open research fund of Songshan Lake materials Laboratory 2021SLABFN11, National Key Research and Development Program of China (Grant No. 2019YFA0705702), OEMT-2021-PZ-02, and Physical Research Platform (PRP) in School of Physics, Sun Yat-sen University. The experiments reported were conducted on the Guangdong Provincial Key Laboratory of Magnetoelectric Physics and Devices (LaMPad).

AUTHOR CONTRIBUTIONS

L.L. and E.Y. carried on the single crystal growth, transport measurements, and contributed equally to this work. E.Y. and B.W. performed the device fabrication. L.L. performed the numeric simulations for device. G.Y. performed transport measurements. B.S. conceived the ideas, contributed to most of the experiments and data processing. B.S., Z.Y., and M.W. discussed and prepared the manuscript.

COMPETING INTERESTS

The authors declare no competing interests.

ADDITIONAL INFORMATION

Supplementary information The online version contains supplementary material available at <https://doi.org/10.1038/s41535-022-00534-7>.

Correspondence and requests for materials should be addressed to Bing Shen, Zhongbo Yan or Meng Wang.

Reprints and permission information is available at <http://www.nature.com/reprints>

Publisher's note Springer Nature remains neutral with regard to jurisdictional claims in published maps and institutional affiliations.



Open Access This article is licensed under a Creative Commons Attribution 4.0 International License, which permits use, sharing, adaptation, distribution and reproduction in any medium or format, as long as you give appropriate credit to the original author(s) and the source, provide a link to the Creative Commons license, and indicate if changes were made. The images or other third party material in this article are included in the article's Creative Commons license, unless indicated otherwise in a credit line to the material. If material is not included in the article's Creative Commons license and your intended use is not permitted by statutory regulation or exceeds the permitted use, you will need to obtain permission directly from the copyright holder. To view a copy of this license, visit <http://creativecommons.org/licenses/by/4.0/>.

© The Author(s) 2023, corrected publication 2023